ACS APPLIED POLYMER MATERIALS

pubs.acs.org/acsapm Article

Imparting High Conductivity to 3D Printed PEDOT:PSS

Ian M. Hill,[▽] Victor Hernandez,[▽] Bohao Xu,[▽] Josiah A. Piceno, John Misiaszek, Adrian Giglio, Emily Junez, Jiajun Chen, Paul D. Ashby, Robert S. Jordan, and Yue Wang*

Cite This: https://doi.org/10.1021/acsapm.3c00232 Read Online

ABSTRACT: Complex 3D geometry and high conductivity have generally been mutually exclusive characteristics for conducting polymers. For instance, poly(3,4-ethylenedioxythiophene):poly(styrenesulfonate) (PEDOT:PSS), a benchmark conducting polymer, typically exhibits conductivity 1 to 2 orders of magnitude lower in 3D-printed forms compared to 2D-processed thin films, due to its sensitivity to processing conditions. Here, we investigate the main causes of this reduced conductivity, which are found to be (1) the ink formulation strategy and (2) the strong lateral phase separation of the printed filaments. Processing approaches that overcome these factors have produced significant conductivity enhancement to 1200 S/cm, higher than the typical 2D-processed PEDOT:PSS. Our study also unveils a set of guiding principles for optimizing the conductivity of direct ink writing (DIW)-printed PEDOT:PSS, including printing orientation, print bed temperature, and nozzle diameter. With the combination of high conductivity and 3D geometric freedom, potential applications such as omnidirectionally deformable LED devices with strain-independent electrical behavior and bespoke electronics that replicate the shape of human body parts have been demonstrated.

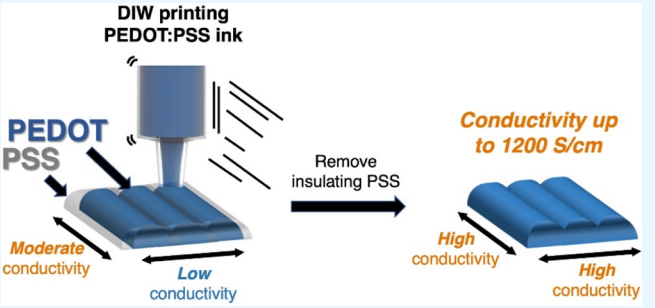

KEYWORDS: *3D printing, direct ink write, phase separation, conducting polymers, PEDOT:PSS*

1. INTRODUCTION

Three-dimensional (3D) printing offers a range of benefits, such as geometric freedom, rapid prototyping, and additive patterning capabilities, across fields including automotive, aerospace, robotics, biomedicine, and electronics.[1−3] While the use of 3D printing technology has become widespread, the challenges of printing organic electronic materials like conjugated, conducting polymers (CPs) persist. This is mainly due to the delicate nature of CPs, which are sensitive to chemical, thermal, and processing conditions.[4] The electron-rich nature of CPs makes them prone to irreversible oxidation or decomposition at elevated temperatures, rendering them incompatible with 3D printing mechanisms such as fused deposition modeling (FDM) or selective laser sintering (SLS), which rely on elevated temperature to produce parts from molten or semimolten polymers.[5−7] Furthermore, even at short chain length, CPs absorb strongly in the ultraviolet and visible wavelength range,[8,9] hindering photoinitiation in light-based 3D printing methods such as stereolithography (SLA) and digital light processing (DLP).[10]

A number of methods, primarily utilizing composite materials or secondary networks, have been used to generate 3D structures with CPs.[11−16] However, the electrical properties of the resulting materials are generally poor due to the insulating additives or chemical modification that improve printability but reduce conductivity. Several recent reports have shown that, among the major 3D printing technologies, direct ink writing (DIW) yields the best electrical performance retention for CPs.[17−19] CPs' solution processability and shear-thinning behavior make them suitable for a shear-based extrusion mechanism of DIW. In particular, poly(3,4-ethylenedioxythiophene):poly(styrenesulfonate) (PEDOT:PSS) (Figure 1b) is the most heavily investigated CP due to its high conductivity and its wide applications in organic electronics, optoelectronics, and bioelectronics.[20−22] However, CPs' sensitivity to processing conditions is clearly reflected in their significantly lower conductivity when 3D printed compared to conventional 2D methods. For example, spin-coated PEDOT:PSS has a conductivity of nearly 1000 S/cm, making it the benchmark material in organic electronic devices.[20−22] However, its DIW-printed counterparts typically have conductivity values ranging between 1 and 155 S/cm in the solid state.[16−19,23,24] Most of these reports retain the printed PEDOT:PSS in the as-processed *hydrogel* form for bioelectronics applications, such as pressure sensors or soft neural probes, for which moderate conductivity in the range of 0.1−50

Received: February 5, 2023
Accepted: May 3, 2023

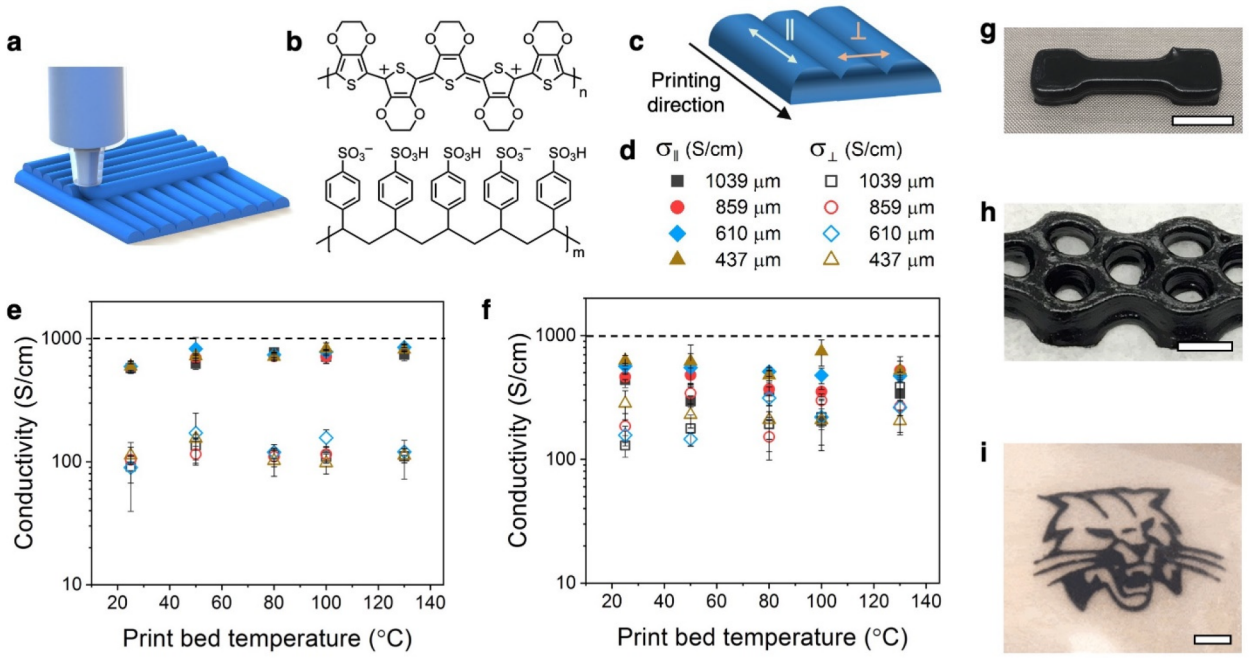

Figure 1. Conductivity of 3D printed PEDOT:PSS. (a) Schematic for direct ink write. (b) Chemical structure for PEDOT:PSS. (c) Schematic illustration showing the parallel (∥) and perpendicular (⊥) directions with respect to the printing direction. (d) Legend for conductivity plots of printed (e) single lines and (f) films (composed of 10 lines). Dashed lines on (e) and (f) denote the benchmark 1000 S/cm conductivity for spin-coated PEDOT:PSS. Photographs of 3D printed PEDOT:PSS: dog bone (g), connected wells (h), and bobcat embedded in silicone (i). Scale bar for (g–i): 10 mm.

S/cm is satisfactory.[12,17−19] However, high conductivity, ideally equal to or exceeding the benchmark value of 1000 S/cm for PEDOT:PSS,[20] is necessary to reach the full potential of 3D printing in high performance, solid-state organic electronics, such as organic photovoltaics or field effect transistors. Reaching this milestone is crucial for advancing the field of 3D organic electronics.

We aim to address the challenge of inferior conductivity in DIW printed PEDOT:PSS by first gaining a fundamental understanding of the factors causing it. We then use this knowledge to improve the conductivity of 3D PEDOT:PSS to surpass that of its 2D thin film counterparts. The combination of intricate geometry and high conductivity in the resulting PEDOT:PSS has the potential to enable new applications, such as organic electronics with geometries that can fill unused spaces, electronics that merge with art, and personalized biomedical devices through integration of 3D scanning and printing.

2. EXPERIMENTAL SECTION

2.1. Ink Preparation. For a typical ink, 100 mL of aqueous PEDOT:PSS dispersion (Clevios PH 1000, 1−1.3 wt % solid content) was added to a 600 mL beaker containing a magnetic stir bar. 5.3 mL (5 vol %) of DMSO (Fisher Scientific) was added to the solution while stirring. The mixture was stirred and heated at 70 °C until it reached a concentration of 3 wt %, at which point it became a viscous paste. It was left to cool at room temperature for 20 min prior to being pressed through a filtration membrane composed of 16 layers of overlapping cheesecloth followed by a polyester filter with a 500 μm wide mesh opening (Elko Filtering Co.) to remove aggregates. The ink is then homogenized in a planetary centrifugal mixer (Thinky AR-100) for 4 min, followed by a 30 s defoaming cycle. The ink is left undisturbed for approximately 10 min to cool to room temperature before syringe loading.

2.2. CAD. CAD models for the prints were created using Autodesk Fusion 360 and Solidworks. The CAD illustrations in the manuscript were sketched using Solidworks, Rhinoceros 3D, or Autodesk 3DS Max. G-codes for single-material and multimaterial prints were generated using Ultimaker Cura Slicer and PrusaSlicer, respectively.

2.3. Printer Modification. Aside from the objects shown in Figure 4, all remaining samples in this work were printed using a Discov3ry Complete Paste Extruder (Structur3D) coupled to an Ultimaker 2+ to enable piston-based DIW printing. A number of machine modifications were carried out to optimize the printer setup for our ink, as detailed in Supplementary Section 1.

2.4. 3D Printing Parameter Tuning. In a typical print, the PEDOT:PSS ink was loaded into a 20 mL luer-lok syringe (Kinesis), which was inserted into the external carriage of the Discov3ry extruder. The syringe and an extrusion nozzle (Subrex) of select gauge size was connected by a ca. 230 mm-long Tygon tubing (Thermo Scientific, 3.175 mm inner diameter) using male and female hosebarb adapters (Cole-Parmer, 3.2 mm inner diameter; part numbers: male: EW-30800-24 and female: EW-30800-08). A print speed of 16 mm/s was used for most prints unless otherwise stated. The optimization process for line dimensions was discussed in Supplementary Section 4.

2.5. Multimaterial Printing. A Cellink Bio X 3D Bioprinter with three 10 mL, temperature-controlled printheads was used for printing the objects shown in Figure 4. Additional details are described in Supplementary Section 10.

2.6. 3D Scanning. A Sense 3D Scanner (3D Systems) was used to scan the hand of a volunteer. The scanned file was subsequently exported as an STL file using the manufacture software. A blender was then used to improve the surface smoothness of the scan by averaging the angles between the polygon faces of the model.

2.7. Postprinting Processing. In a typical postprinting solvent treatment experiment, 50 mL of DMSO in a covered Pyrex crystallizing dish was preheated to 100 °C and magnetically stirred. Fully dried samples that were printed on either glass slides or silicon wafers were placed into the covered DMSO bath that were gently stirring at a speed of 50 rpm for 20 min. The PEDOT:PSS prints delaminated from their substrates during the process. The swelled prints were then carefully removed from the solvent by adhering them to the desired substrates

https://doi.org/10.1021/acsapm.3c00232
ACS Appl. Polym. Mater. XXXX, XXX, XXX−XXX

and slowly pulled out of the bath. The edges of the substrates were then tilted and pressed onto several layers of Kimwipes to remove excess DMSO, and the remaining trace amount of visible DMSO on the substrate was absorbed with the corner of a Kimwipe. The samples were then annealed at 130 °C for 10 min on a hot plate.

2.8. Conductivity Measurement. A Keithley 2450 SMU SourceMeter with a Keithley Model 5806 Kelvin Clip Lead Set was used to measure the four-terminal resistances of two-lead samples. Additional details are described in Supplementary Section 4.

2.9. Material Characterization. Tensile and compression stress−strain and fatigue tests were carried out using an Instron 3369 universal machine equipped with a 100 N load cell. Rheology characterizations were performed on an Anton Paar MCR 102 rheometer at room temperature. Testing parameters were detailed in Supplementary Section 2. Experimental details for wide-angle X-ray scattering (WAXS), atomic force microscopy (AFM), scanning electron microscopy (SEM), and X-ray photoelectron spectroscopy (XPS) are discussed in Supporting Sections 6, 6, 4, and 7, respectively.

3. RESULTS AND DISCUSSION

3.1. Ink Formulation and DIW Printing. Two key rheological requirements of printable inks for DIW are shear thinning and moderate yield stress. Shear thinning enables the ink to flow under shear force during extrusion, while moderate yield stress allows the extruded ink to retain its shape and stack vertically.[1] These rheological properties are typically associated with viscous polymer solutions or dispersions. The as-purchased PEDOT:PSS aqueous colloidal dispersion has a solid content of 1−1.3 wt % and low viscosity, making it unsuitable for DIW (Figures S4 and S5). To circumvent this issue, previous reports reformulated the PEDOT:PSS dispersion through lyophilization followed by redistribution, used a gelation agent, or carried out *in situ* polymerization in the presence of another polymer network.[12,17,19] We hypothesize that the lower conductivity of PEDOT:PSS from these formulation strategies compared to spin-coated or drop-casted 2D thin films may be partially due to the impact of processing methods, solvents, additives, and other conditions on chain conformation, packing arrangement, crystallinity, and phase separation of PEDOT:PSS, which are factors that affect the electrical properties of CPs. Therefore, imitating the natural solvent evaporation process of spin coating or drop casting in preparing the DIW ink will increase the likelihood of achieving high conductivity in the printed PEDOT:PSS. As a result, we prepared a DIW-printable ink by simply mixing 5 vol % of dimethyl sulfoxide (DMSO), the most commonly used "secondary dopant" for PEDOT:PSS,[20] into the as-purchased aqueous dispersion, followed by slowly evaporating the solvent under gentle heating. We found that concentrating the PEDOT:PSS dispersion to 3 wt % has the most desirable rheological properties for DIW printing (Figures S4 and S5). Additionally, we found that a piston-based DIW extrusion mechanism is more suitable than the more commonly used pneumatic mechanism for this ink formulation,[1] due to its insensitivity to the ink's gradual increase in yield stress over time (Figure S6). These are the conditions and method we chose for this study.

With parameter optimization (Figure S7), we were able to demonstrate good resolution control for printed lines where their widths are nearly identical with the nozzle inner diameter for nozzle sizes ranging from 50 to 1039 μm (Figures S7e and S8). Six to ten layers of this ink can be stacked to form a variety of freestanding or encapsulated 3D structures (Figure 1g−i). Drying of the printed specimen leads to solid PEDOT:PSS. Scanning electron microscopy (SEM) images of a single-layer, solid PEDOT:PSS film show that adjacent filaments are merged together with no distinguishable interfaces along the cross sections (Figure S9). This is likely a result of the high water content of the PEDOT:PSS ink and the slow drying rate, which provides sufficient mobility and time for chains to diffuse and merge at the interfaces between adjacent filaments.

3.2. Conductivity. To thoroughly understand the processing−structure−electrical property relations of the 3D printed PEDOT:PSS, we carried out a series of conductivity measurements based on the following rationale. (1) Since shear-based directional processing is often associated with anisotropic physical properties,[25−28] conductivities were measured in the directions parallel (∥) and perpendicular (⊥) to the printing direction, denoted as $\sigma_{\parallel}$ and $\sigma_{\perp}$, respectively (Figure 1c). (2) DIW 3D printing involves the extrusion of 1D filaments arranged into 2D layers, which are then vertically stacked into 3D structures. To understand the effect of this additive nature on the electrical properties of PEDOT:PSS, the conductivity anisotropy was analyzed for both single extruded lines and films that comprise ten slightly overlapping parallel lines. (3) During DIW extrusion, the ink experiences shear thinning, which is associated with domain alignment and/or chain extension or alignment.[29] A smaller nozzle diameter results in a higher shear force. Therefore, conductivity is measured for PEDOT:PSS extruded using a range of nozzle sizes. Finally, (4) substrate temperature has been shown to influence the degree of crystallinity and phase separation in solution-processed CPs.[30] Hence, to investigate the relationship between substrate temperature and CP conductivity, the printing process was performed using different print bed temperatures. The results from these measurements are shown in Figure 1d−f.

Conductivity of the single extruded filaments best represents the electrical properties directly induced by the extrusion process (Figure 1d,e). Significant conductivity anisotropy between $\sigma_{\parallel}$ and $\sigma_{\perp}$ is observed for all printed filaments. Interestingly, the conductivity values, regardless of measurement directions, have negligible correlation with nozzle diameter. Also, both $\sigma_{\parallel}$ and $\sigma_{\perp}$ exhibit a minor dependence on print bed temperature. The $\sigma_{\parallel}$ increases from ca. 576 to 851 S/cm and $\sigma_{\perp}$, from ca. 91 to 120 S/cm as the print bed temperature increases from 25 to 130 °C. We emphasize that the higher end of $\sigma_{\parallel}$ for our printed PEDOT:PSS approaches the benchmark value of 1000 S/cm even in the as-printed form. These results demonstrate that high conductivity can be achieved in 3D printed CPs through ink preparation methods that mimic the conditions leading to high conductivity in 2D processing.

For DIW-printed films composed of ten parallel, slightly overlapping lines, the anisotropy between $\sigma_{\parallel}$ and $\sigma_{\perp}$ largely diminishes, but $\sigma_{\parallel}$ remains consistently higher than $\sigma_{\perp}$ within each film (Figure 1d,f). The $\sigma_{\parallel}$ for each film is lower than the single filament counterpart, whereas the $\sigma_{\perp}$ follows the opposite trend. Films printed with the high print bed temperature exhibit less conductivity anisotropy than those from low print bed temperature.

3.3. Mechanistic Investigation. To uncover the source of these conductivity trends, we investigate how printing parameters impact the key factors that influence electrical properties of PEDOT:PSS: (1) chain alignment, (2) nanoscopic morphology, (3) crystallinity, and (4) phase separation.

Processing methods that involve directional shear flow are often reported to induce a certain degree of polymer chain or nanoscopic domain alignment.[29] This led us to investigate whether the shear from DIW printing induces polymer chains or

https://doi.org/10.1021/acsapm.3c00232
ACS Appl. Polym. Mater. XXXX, XXX, XXX−XXX

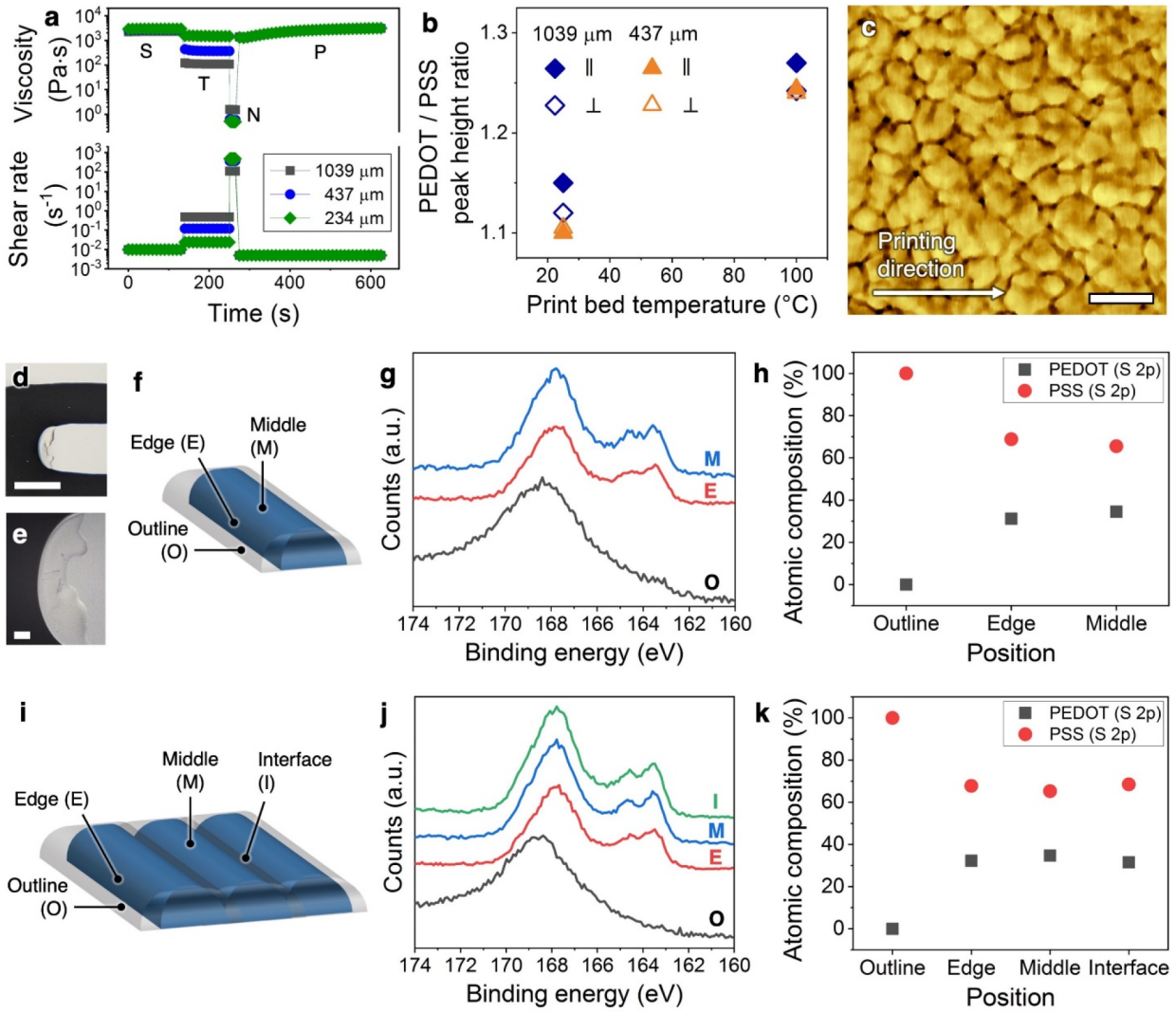

Figure 2. Structure–property relations and phase separation of 3D printed PEDOT:PSS. (a) Rheological experiment simulating the DIW process collected in steady-shear condition. The S, T, N, and P symbols correspond to the travel path of PEDOT:PSS ink and the associated conformational changes of PEDOT:PSS complexes under flow in the syringe, tubing, nozzle, and post-extrusion, respectively. (b) Height ratios of the PEDOT (020) ($q \approx 1.8$ Å^{-1}) and PSS ($q \approx 1.2$ Å^{-1}) peaks from integrated 1D intensities of WAXS spectra along the parallel direction of films printed using different nozzle diameters. (c) AFM phase image for film printed with a bed temperature of 100 °C using a nozzle with an inner diameter of 437 μm. Scale bar: 100 nm. (d, e) Optical microscope images showing the visible phase separated PSS (clear substance) from the PEDOT:PSS filament. Scale bars: 200 μm. (f) Schematic drawing showing the different regions of a single printed line and (g) XPS spectra for these regions. The integrated atomic composition for PEDOT and PSS at these regions is shown in (h). (i) Schematic drawing showing the different regions of a printed film. The corresponding XPS spectra and the integrated atomic composition are shown in (j) and (k), respectively.

domains to uncoil and/or deform and reorient along the flow direction, leading to anisotropic conductivity. To probe this hypothesis, we carried out rheological experiments to simulate the extrusion process.[31] We found that the viscosity and storage moduli recover rapidly within approximately 20 s for all nozzle diameters, which is faster than the time it takes for the printed ink to dry (Figures 2a and S12). From this, we can conclude that shear-induced alignment is not a significant contributor to the observed anisotropic conductivity,[32] which explains the lack of dependence of conductivity on nozzle diameter.

Wide angle X-ray scattering (WAXS) was employed to further elucidate the origins of the weak dependence of PEDOT:PSS conductivity on substrate temperature and the lack of correlation between nozzle size and conductivity. Higher print bed temperature leads to an increase in PEDOT π–π stacking peak intensity ($q \approx 1.8$ Å) and, hence, a higher PEDOT-to-PSS peak ratio and crystallite size (Figures 2b and S14). This is consistent with those from prior literature which illustrated that elevated solvent evaporation rates, resulting from higher substrate temperature, improves the ordering of solution processed CPs, thus increasing conductivity.[32] However, little difference in PEDOT π–π peak intensity, and hence PEDOT-to-PSS peak ratio, is observed between PEDOT:PSS printed using different nozzle sizes (Figures 2b and S14a), nor is there any anisotropy in peak intensity or crystallite sizes (Figures S13 and S14b). Additionally, little directionality is observed at the nanoscopic domain scale, evidenced by the near-spherical fast Fourier transform (FFT) patterns of the AFM images (Figures 2c and S15). These results are consistent with the findings of rheological simulation, which indicated that the chains or domains relax back to the isotropic state rapidly after shear force is removed.

https://doi.org/10.1021/acsapm.3c00232
ACS Appl. Polym. Mater. XXXX, XXX, XXX–XXX

3.4. Phase Separation. The minor crystallographic and morphological anisotropies cannot account for the significant conductivity anisotropy, with a difference as large as 730 S/cm between $\sigma_{\parallel}$ and $\sigma_{\perp}$ (Figure 1e). We noticed that one distinct feature of these DIW-printed PEDOT:PSS is that they have unusually strong phase separation. Transparent outlines around the printed specimen can often be visibly observed, particularly around corners where the capillary force is especially strong (Figure 2d,e). Some of these transparent outlines are large enough (3−5 mm in width) to be isolated for WAXS and X-ray photoelectron spectroscopy (XPS) analyses, both of which confirm its identity as PSS (Figure S16).[33,34]

To understand the effect of phase separation on sample conductivity, XPS was employed to probe the chemical composition at different locations of the printed filaments (Figure 2f−h) and films (Figure 2i−k). For PEDOT:PSS, two sets of distinct peaks are observed in XPS: doublets at 163.7 and 165.4 eV, arising from the S $2p_{1/2}$ and S $2p_{3/2}$ of the thiophene in PEDOT, and the higher binding energy peak centered at around 167.8 eV, which is the sum of the 167.6 eV (S $2p_{1/2}$) and 168.9 eV (S $2p_{3/2}$) constituents of the sulfonate sulfur in PSS.[34,35] For single printed lines, XPS revealed different chemical composition at the middle, edge, and outline (i.e., area immediately adjacent to the filament edge), denoted as M, E, and O, respectively (Figure 2f). Each filament is surrounded by a pure PSS outline on the sides (Figure 2g,h). The absence of the inductive effects from positively charged PEDOT causes the PSS peak in the outline to appear at a higher binding energy (168.6 eV) than that in PEDOT:PSS, confirming that the PSS chains in the outline are unbound to PEDOT.[36] Integrating the areas under peaks reveals that the PEDOT content is slightly higher in the middle of the filament (ca. 35%) than near the edges (ca. 31%) (Figures 2h and S17).

The likely cause of this strong lateral phase separation is the drying kinetics of the printed specimen. While the shear-based DIW 3D printing mechanism bears resemblance to brush painting or solution shearing, the drying kinetics of the 3D printed PEDOT:PSS is similar to drop-casted films. The nozzle diameters used in our study varied from 50 to 1039 μm, leading to filaments of a PEDOT:PSS paste of width similar to the nozzle diameters (because the bottom of the filaments are pinned to the substrate) but shrinking in the height direction to 25 to 35 μm upon complete drying. This thickness range is similar to that of drop-casted films but diverges significantly from the spin-coated, brush painted, or solution sheared counterparts, which have thickness of tens to hundreds of nanometers. As a result, the time scale for drying is significantly longer for 3D printed samples than those from 2D shear-based methods. The as-purchased PEDOT:PSS formulation has a PEDOT-to-PSS ratio of 1-to-2.2 because excess PSS is necessary to offset the poor water-solubility of PEDOT to create a stable colloidal dispersion. Previous work has shown that ∼73% of PSS is associated with PEDOT through electrostatic interaction, indicating the presence of a substantial amount of free PSS.[37] Prior to concentrating the ∼1 wt % PEDOT:PSS aqueous dispersion to a 3 wt % printable ink, 5 vol % of DMSO was added for conductivity enhancement. DMSO has a low vapor pressure and does not form azeotropes with water.[38] Therefore, as water evaporates, the DMSO concentration in solvent consistently increases. Hence, the 3 wt % PEDOT:PSS aqueous ink likely has a DMSO concentration of ∼17 vol %. As the extruded filament dries, the DMSO concentration gradually increases due to the decrease in water content. The PEDOT:PSS electrostatic complex can be swelled by, but cannot be dissolved in, the DMSO-rich solvent.[38] On the other hand, the free PSS is soluble in this solvent environment and can be extracted to concentrate in this phase. As a result of this solid−liquid phase separation, PEDOT:PSS complexes precipitate out while the free PSS accumulates in the DMSO-rich solvent on the periphery of the printed lines, leading to strong phase separation, evidenced by the observed chemical compositional differences across the filament width (Figure 2f−h). This proposed mechanism is in agreement with previous findings demonstrating that drying drop-casted PEDOT:PSS containing over 10 vol % DMSO leads to significant radial phase separation with unbound PSS forming a border around the PEDOT:PSS film.[38]

This strong lateral phase separation is likely the cause of the strong conductivity anisotropy in printed filaments (Figure 1e). For $\sigma_{\parallel}$ measurement, the entire width of the printed line is wrapped within the electrodes (Figure S18a). Despite the strong lateral phase separation, efficient charge transport is facilitated by the direct contact of the PEDOT-rich middle section of the line with the electrodes. Conversely, in $\sigma_{\perp}$ measurements, the electrodes are largely in contact with the PSS outline, so the PSS outline and PSS-rich line edges act as barriers that impede efficient charge transport (Figure S19c), leading to substantially lower measured conductivity values.

To probe whether interfilament interfaces in DIW-printed PEDOT:PSS films form resistive barriers between adjacent lines, we analyzed the chemical composition at the interface (I) between adjacent lines in addition to the middle and edge of lines and the outline of the film (Figure 2i). As shown in the stacked XPS spectra and the integrated atomic composition plot (Figure 2j,k), a pure PSS outline is observed at the periphery of the film. The PEDOT composition at the line edge and the interface between adjacent lines are similar, 32% and 31%, respectively, which is slightly lower than the 35% PEDOT content at the middle of the line. Considering the drying time for filaments is likely on the order of hundreds of seconds[32] and the printing speed is 16 mm/s for printing structures that are typically 20−60 mm in length, the newly extruded filament is likely deposited on a hydrated previously deposited filament. The absence of a significantly more PSS-rich region at the line interfaces suggest that the adjacent lines merge while they are still hydrated before the lateral phase separation could occur within individual filaments, meaning less PSS separates into its own phase. Consequently, we conjecture that the printed PEDOT:PSS films contain more free PSS across its volume, beyond the surface depth that XPS can profile, than the single printed lines. This could explain the weaker conductivity anisotropy in films where their $\sigma_{\parallel}$ values are lower than those in their respective single-line counterparts (Figure 1f).

3.5. Postprinting Treatment for Further Conductivity Enhancement. With the knowledge that strong phase separation is the main cause for lowered conductivity and strong anisotropy in DIW 3D printed PEDOT:PSS films, we carried out a postprinting solvent treatment to remove the PSS outline. A number of polar organic solvents, including short-chain alcohols or their mixtures, DMSO, ethylene glycol, and aqueous acid solutions, have been shown to be effective solvents in removing unbound PSS.[20] We chose DMSO as the rinsing solvent to be consistent with the solvent additive incorporated in the initial DIW ink preparation to avoid additional variables.

Using the 1039 μm nozzle as a case-study, XPS analyses confirm the complete removal of the pure PSS outline at the filament and film periphery and some unbound PSS within the

https://doi.org/10.1021/acsapm.3c00232
ACS Appl. Polym. Mater. XXXX, XXX, XXX−XXX

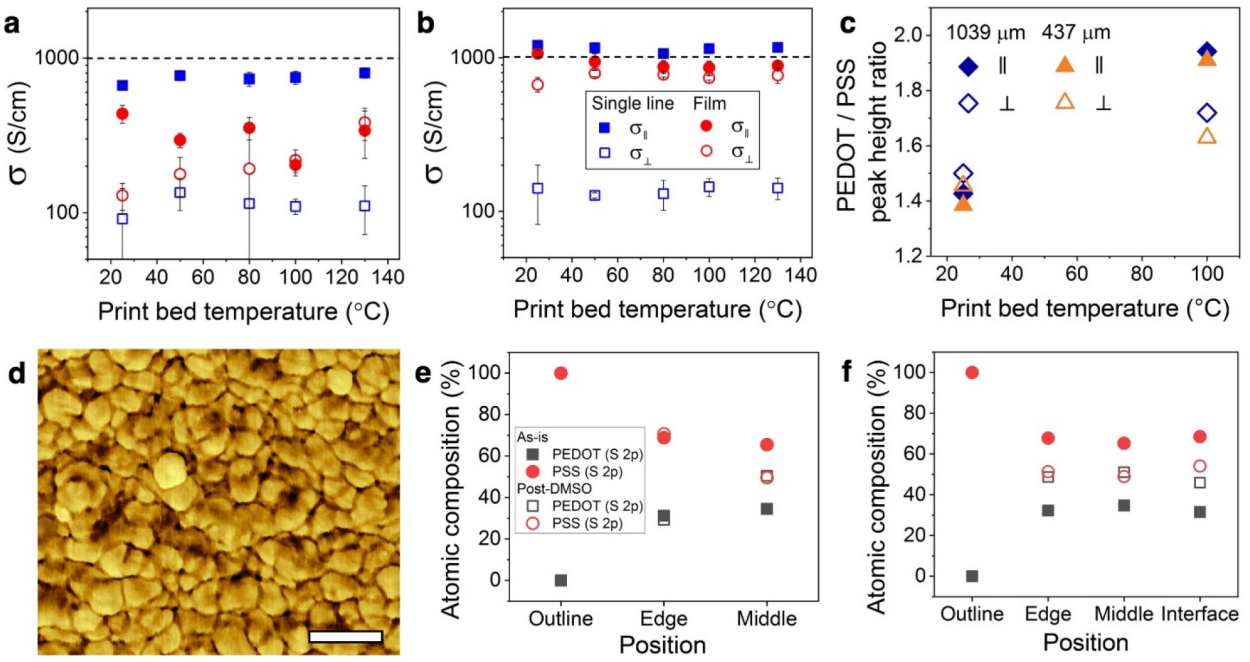

Figure 3. Properties of 3D printed PEDOT:PSS after DMSO treatment. (a) Conductivity along the parallel and perpendicular directions for as-printed dried PEDOT:PSS single lines and films extruded using a 1039 μm nozzle. (a) shares the same legend as (b). (b) Conductivity for PEDOT:PSS single lines and films printed using a 1039 μm nozzle after DMSO treatment. (c) Height ratios of the PEDOT (020) ($q \approx 1.8$ Å) and PSS ($q \approx 1.2$ Å) peaks. (d) AFM phase image for post-DMSO-treated PEDOT:PSS film printed with a bed temperature of 100 °C using a nozzle with an inner diameter of 437 μm. Scale bar: 100 nm. The integrated PEDOT and PSS atomic compositions from XPS analyses for DMSO-treated single lines and films are shown in (e) and (f), respectively. (e) and (f) share the same legend.

PEDOT:PSS (Figures 3e,f, S23, and S24). The anisotropic conductivity data for as-printed single lines and films printed using the 1039 μm nozzle are isolated in Figure 3a, where the different sets of values scattered across a nearly 1 order of magnitude range. In stark contrast, after DMSO treatment, the $\sigma_{\parallel}$ for single lines and films and the $\sigma_{\perp}$ for films all converged to the ca. 1000 S/cm region (Figure 3b). Notably, the $\sigma_{\parallel}$ values for the DMSO-treated single lines, regardless of print bed temperature, are all above the benchmark 1000 S/cm value, with values as high as ca. 1200 S/cm. WAXS and AFM also confirm that the mechanism for this increase in conductivity and decrease in anisotropy is the removal of free-PSS through DMSO rinsing (Figures S20−S23).

Interestingly, the $\sigma_{\perp}$ values for post-DMSO treated single lines remain approximately the same as those for the as-printed samples. This can be attributed to the mostly unchanged PEDOT-to-PSS ratio at the line edges (Figure 3a,e). The higher PSS content at the edges could be a result of the higher edge-to-volume ratio in single lines compared to films. This causes the PSS-containing DMSO to collect at filament edges due to the higher capillary force, which may have resulted in the dissolved PSS to be reabsorbed into the edges during drying. Additional rinsing steps with fresh DMSO or other solvents may alleviate this lateral compositional difference. Given the emphasis of this study is to identify the source of low conductivity and reach the 1000 S/cm benchmark conductivity in DIW-printed PEDOT:PSS, we elected not to focus on post-treatment optimization.

3.6. Demonstrations for 3D Applications. The 3D printing of PEDOT:PSS with conductivity surpassing 1000 S/cm in the solid state opens new opportunities in several previously inaccessible applications. We demonstrate such prospects with two examples (Figure 4).

3D printing, in combination with 3D scanning, has led to replicas of physiologically accurate organs and limbs that can serve as surgical practice objects, tissue engineering platforms, and bespoke prosthetics.[39−41] The high conductivity and low impedance of PEDOT:PSS have rendered it a sought-after material in cell culture platforms or probes for stimulation, sensing, and recording for electro-responsive cells such as neurons or cardiomyocytes.[41−43] To demonstrate the prospect of combining these two fields, we 3D scanned a hand and used DIW to print the output CAD file into a PEDOT:PSS replica (Figures 4a−c and S26). This demonstration illustrates the potential to create electro-responsive artificial organs and personalized functional organic prosthetics.

Stretchable and wearable electronics is another area where highly conductive, 3D printed PEDOT:PSS can create new opportunities. These electronics need to retain electrical functions under mechanical deformation such as stretching and flexing, ideally omnidirectionally.[44,45] CPs are one of the main classes of materials for such *de novo* electronics.[46,47] However, the intrinsically brittle CPs such as PEDOT:PSS need to be chemically modified or blended with an additive to become stretchable.[46,47] Aside from their often inferior conductivity in the unstrained state resulting from these modifications, the conductivity of these materials is often also heavily strain dependent because polymer chains or nanoscopic domains need to deform to accommodate strain.

3D printing brings the capability to create structures that can accommodate mechanical deformation through 3D geometry, which effectively decouples materials' electrical properties from its response to mechanical deformation.[11,48] We utilize multi-material DIW to print PEDOT:PSS springs with the support of a sacrificial material, Pluronic F-127 hydrogel (Figure 4d,e).[49] Support removal followed by dehydration produces solid

https://doi.org/10.1021/acsapm.3c00232
ACS Appl. Polym. Mater. XXXX, XXX, XXX−XXX

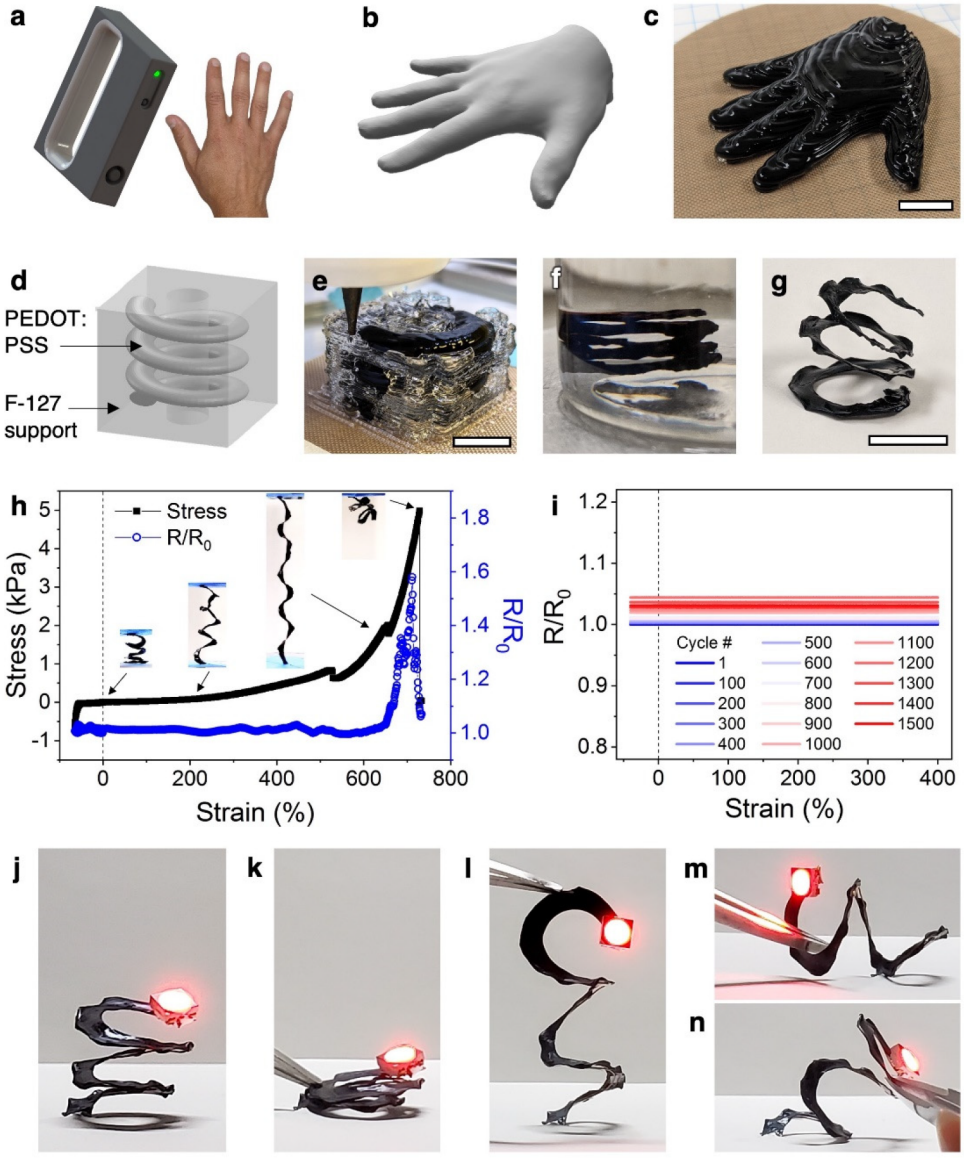

Figure 4. New applications enabled by 3D printed PEDOT:PSS. (a–c) Demonstration showing the prospect for 3D scanned, personalized organic bioelectronics. (a) Schematic illustration of the 3D scanning of a hand. (b) CAD output for the 3D scanned hand. (c) 3D printed PEDOT:PSS replica of the hand in the hydrated state. (d–n) Omnidirectional mechanically flexible, compressible, and stretchable organic electronics with high stability. (d) CAD schematic illustration showing a three-turn PEDOT:PSS spring embedded in F-127 support. (e) Multimaterial DIW printing of the structure shown in (d). (f) Freestanding PEDOT:PSS hydrogel after the dissolution of the F-127 support. (g) Freestanding solid-state PEDOT:PSS spring upon dehydration. (h) Stress–strain-normalized resistance relations of the spring being compressed to 60% strain and returned to 0% strain, followed by elongation until failure. A 500%/min strain rate was used. (i) Normalized resistance of the spring as it is cycled between 40% compression and 400% elongation for 1500 cycles. (j–n) An LED electronic device using the PEDOT:PSS spring as an interconnect being compressed, stretched, and flexed in various directions while retaining its emission intensity. Scale bars for (c), (e), and (g): 10 mm.

PEDOT:PSS springs (Figure 4f,g). These solid-state springs typically exhibit some defects such as edge rippling. We note that the isotropic dehydration and shrinking of hydrogel structures is a challenge in the 3D printing field and the subject of several recent standalone, notable studies.[50−52] Protocols for uniformly dehydrating PEDOT:PSS hydrogels with complex 3D shapes have not been reported to the best of our knowledge. Hence, our dehydration process focuses on general shape retention rather than perfecting the retention of geometry and resolution.

The solid springs can be elastically compressed to −65% strain (negative sign denotes compressive strain) and elongated up to ∼700% strain (inset to Figure 4h and Movie S1). A nearly plateau stress–strain regime, characteristic to the structural expansion and rotation in cellular or 3D architected materials, occurs between −55% and 450% strain. Since little stress is exerted on polymer chains or domains in this regime, the resistance of the spring is nearly unchanged (<4.5% increase) after 1000 cycles between −40% and 400%, demonstrating the remarkable electrical stability and fatigue resistance imbued by 3D geometries (Figures 4i and S28). Such electrical–mechanical correlations are further illustrated through a highly omnidirectionally deformable LED device that retain light intensity through compression, stretching, bending, and twisting (Figures 4j–n and S30 and Movie S2). The advantageous attributes of 3D-shaped PEDOT:PSS are in stark contrast to previous work that relies on chemical modification, additives, or

https://doi.org/10.1021/acsapm.3c00232
ACS Appl. Polym. Mater. XXXX, XXX, XXX−XXX

composites, which exhibit resistance changes starting at as low as 5% tensile strain and by several folds when elongated to 50−100% strain.[46,47] The ability to process CPs in 3D provides the flexibility and opportunity to access more elaborate and tunable geometry−stress−strain−electrical property relations, such as those associated with complex 3D architected metamaterials,[11,48] providing a new approach for creating mechanically deformable or reconfigurable organic electronic materials.

4. CONCLUSIONS

The findings from this work have unveiled a number of fundamental insights for the DIW 3D printing of PEDOT:PSS, in particular, that the cause for its low conductivity associated with DIW processing is the strong lateral phase separation. We demonstrated that conductivity as high as 1200 S/cm can be achieved in 3D-printed PEDOT:PSS by (1) formulating DIW ink under conditions that resemble conventional 2D processing and (2) removing the free PSS at filament periphery from the lateral phase separation. PEDOT:PSS-based electronics with new form factors have been achieved as a result of our study.

Our investigation has also offered a number of other fundamental insights for creating highly conductive 3D PEDOT:PSS. First, for both single lines and films, $\sigma_{\parallel}$ is consistently higher than $\sigma_{\perp}$ even after DMSO rinsing, albeit the difference is small in films. This feature indicates that, if achieving the lowest possible resistance is paramount to an application, the printing direction should be aligned with the direction of current flow. Second, the conductivity dependence on print bed temperature is also mostly removed after DMSO treatment. Therefore, DIW printing can be carried out at room temperature to achieve high conductivity for process simplicity. Third, we found that the conductivity of DIW printed PEDOT:PSS is largely independent of nozzle diameter. After the postprinting solvent treatment, single line conductivity is still slightly higher than their film counterparts. Therefore, for the printing of an electrode or interconnect of a certain width, it is advantageous to print using a nozzle that matches the line width rather than printing multiple overlapping lines using smaller nozzles. Applying these insights can potentially lead to more efficient charge transport in 3D printed organic electronics containing PEDOT:PSS.

■ ASSOCIATED CONTENT

Supporting Information

The Supporting Information is available free of charge at https://pubs.acs.org/doi/10.1021/acsapm.3c00232.

Modifications made to the DIW 3D printer, PEDOT:PSS ink optimization, time dependence of the rheological properties for PEDOT:PSS ink, printing parameter optimization, optical microscope images of freshly printed PEDOT:PSS, optical and SEM images of filament interfaces within DIW printed PEDOT:PSS films, comparison between two-contact resistance measurements using Keithley 5806 K clamps and four-point resistance measurement geometries, rheology simulation for the printing of PEDOT:PSS ink, additional crystallographic and morphological characterization, explanation of the relationship between phase separation and conductivity, additional WAXS characterization for DMSO-treated films, additional data on the effect of DMSO treatment on phase separation, and demonstrations for applications (PDF)

Movie S1: 3D printed PEDOT:PSS spring under compression and tension (MP4)

Movie S2: Omnidirectionally deformable LED device (MP4)

■ AUTHOR INFORMATION

Corresponding Author

Yue Wang − *Department of Materials Science and Engineering, University of California, Merced, California 95343, United States; Department of Chemistry and Biochemistry, University of California, Merced, California 95343, United States;* orcid.org/0000-0002-1412-1618; Email: yuewang@ucmerced.edu

Authors

Ian M. Hill − *Department of Materials Science and Engineering, University of California, Merced, California 95343, United States*

Victor Hernandez − *Department of Materials Science and Engineering, University of California, Merced, California 95343, United States*

Bohao Xu − *Department of Materials Science and Engineering, University of California, Merced, California 95343, United States*

Josiah A. Piceno − *Department of Materials Science and Engineering, University of California, Merced, California 95343, United States*

John Misiaszek − *Department of Materials Science and Engineering, University of California, Merced, California 95343, United States*

Adrian Giglio − *Department of Mechanical Engineering, University of California, Merced, California 95343, United States*

Emily Junez − *Department of Materials Science and Engineering, University of California, Merced, California 95343, United States*

Jiajun Chen − *Molecular Foundry, Lawrence Berkeley National Laboratory, Berkeley, California 94720, United States;* orcid.org/0000-0002-4061-6219

Paul D. Ashby − *Molecular Foundry, Lawrence Berkeley National Laboratory, Berkeley, California 94720, United States;* orcid.org/0000-0003-4195-310X

Robert S. Jordan − *Department of Materials Science and Engineering, University of California, Merced, California 95343, United States;* orcid.org/0000-0001-9780-6091

Complete contact information is available at: https://pubs.acs.org/10.1021/acsapm.3c00232

Author Contributions

[▽]These authors contributed equally: I.M.H., V.H., and B.X. Conceptualization: Y.W.; R.S.J. 3D printing: I.M.H.; J.A.P.; R.S.J. Machine building: J.M. 3D scanning: A.G. Conductivity: I.M.H.; V.H.; B.X.; E.J. Rheology: B.X.; I.M.H. WAXS: V.H. AFM: V.H.; J.C.; P.D.A. SEM: V.H.; B.X. XPS: B.X. Mechanical and electrical testing: V.H.; B.X. Demo: B.X. Writing: I.M.H.; V.H.; B.X.; J.A.P.; J.M.; J.C.; P.D.A.; R.S.J.; Y.W.

Funding

National Science Foundation, CAREER, DMR-1945664 (Y.W.); Arnold and Mabel Beckman Foundation, Beckman Young Investigator Award (Y.W.); University of California, Merced, Start-up fund (Y.W.); Department of Energy, National Nuclear Security Administration, Minority Serving Institution

Partnership Program, Award DE-NA0003866 (E.J.); University of California, Merced, Bridge to Research Program (E.J.)

Notes

The authors declare no competing financial interest.

■ ACKNOWLEDGMENTS

We thank Maria Celeste Castillo and Emily Tran for assistance with CAD and 3D printer setup and Dr. Eric Schaible for collecting some of the WAXS data. XPS and SEM access was provided by the Imaging and Microscopy Facility (IMF) at UC Merced. AFM imaging performed at the Molecular Foundry was supported by the Office of Science, Office of Basic Energy Sciences, of the U.S. Department of Energy under Contract No. DE-AC02-05CH11231. Synchrotron X-ray scattering experiments were performed at Beamline 7.3.3 of the Advanced Light Source, a U.S. DOE Office of Science User Facility under contract No. DE-AC02-05CH11231 and at Beamline 11-3 of the Stanford Synchrotron Radiation Lightsource, SLAC National Accelerator Laboratory, supported by the U.S. Department of Energy, Office of Science, Office of Basic Energy Sciences under Contract No. DE-AC02-76SF00515.

■ REFERENCES

(1) Zhou, L. Y.; Fu, J.; He, Y. A Review of 3D Printing Technologies for Soft Polymer Materials. *Adv. Funct. Mater.* **2020**, *30* (28), 2000187.

(2) Kamyshny, A.; Magdassi, S. Conductive Nanomaterials for 2D and 3D Printed Flexible Electronics. *Chem. Soc. Rev.* **2019**, *48* (6), 1712−1740.

(3) MacDonald, E.; Wicker, R. Multiprocess 3D Printing for Increasing Component Functionality. *Science* **2016**, *353* (6307), aaf2093.

(4) Jordan, R. S.; Wang, Y. 3D Printing of Conjugated Polymers. *J. Polym. Sci. B Polym. Phys.* **2019**, *57* (23), 1592−1605.

(5) Olabisi, O., Adewale, K., Eds. Conductive Thermoplastics. In *Handbook of Thermoplastics*, 2nd ed.; CRC Press, 2016; pp 669−692; DOI: 10.1201/b19190.

(6) Jørgensen, M.; Norrman, K.; Krebs, F. C. Stability/degradation of polymer solar cells. *Sol. Energy Mater. Sol. Cells* **2008**, *92* (7), 686−714.

(7) Louis, B.; Caubergh, S.; Larsson, P. O.; Tian, Y.; Scheblykin, I. G. Light and oxygen induce chain scission of conjugated polymers in solution. *Phys. Chem. Chem. Phys.* **2018**, *20* (3), 1829−1837.

(8) Xia, Y.; Wiesinger, J. M.; MacDiarmid, A. G.; Epstein, A. J. Camphorsulfonic Acid Fully Doped Polyaniline Emeraldine Salt: Conformations in Different Solvents Studied by an Ultraviolet/Visible/Near-Infrared Spectroscopic Method. *Chem. Mater.* **1995**, *7* (3), 443−445.

(9) Zhang, W. J.; Feng, J.; MacDiarmid, A. G.; Epstein, A. J. Synthesis of oligomeric anilines. *Synth. Met.* **1997**, *84* (1), 119−120.

(10) Lopez-Larrea, N.; Criado-Gonzalez, M.; Dominguez-Alfaro, A.; Alegret, N.; del Agua, I.; Marchiori, B.; Mecerreyes, D. Digital Light 3D Printing of PEDOT-Based Photopolymerizable Inks for Biosensing. *ACS Appl. Polym. Mater.* **2022**, *4* (9), 6749−6759.

(11) Jordan, R. S.; Frye, J.; Hernandez, V.; Prado, I.; Giglio, A.; Abbasizadeh, N.; Flores-Martinez, M.; Shirzad, K.; Xu, B.; Hill, I. M.; Wang, Y. 3D printed architected conducting polymer hydrogels. *J. Mater. Chem. B* **2021**, *9* (35), 7258−7270.

(12) Zhang, S.; Chen, Y.; Liu, H.; Wang, Z.; Ling, H.; Wang, C.; Ni, J.; Çelebi-Saltik, B.; Wang, X.; Meng, X.; Kim, H. J.; Baidya, A.; Ahadian, S.; Ashammakhi, N.; Dokmeci, M. R.; Travas-Sejdic, J.; Khademhosseini, A. Room-Temperature-Formed PEDOT:PSS Hydrogels Enable Injectable, Soft, and Healable Organic Bioelectronics. *Adv. Mater.* **2020**, *32* (1), 1904752.

(13) Fantino, E.; Roppolo, I.; Zhang, D.; Xiao, J.; Chiappone, A.; Castellino, M.; Guo, Q.; Pirri, C. F.; Yang, J. 3D Printing/Interfacial Polymerization Coupling for the Fabrication of Conductive Hydrogel. *Macromol. Mater. Eng.* **2018**, *303* (4), 1700356.

(14) Wu, Y.; Chen, Y. X.; Yan, J.; Yang, S.; Dong, P.; Soman, P. Fabrication of conductive polyaniline hydrogel using porogen leaching and projection microstereolithography. *J. Mater. Chem. B* **2015**, *3* (26), 5352−5360.

(15) Joo, H.; Cho, S. Comparative Studies on Polyurethane Composites Filled with Polyaniline and Graphene for DLP-type 3D Printing. *Polymers* **2020**, *12* (1), 67.

(16) Mire, C. A.; Agrawal, A.; Wallace, G. G.; Calvert, P.; Panhuis, M. I. H. Inkjet and extrusion printing of conducting poly(3,4-ethylenedioxythiophene) tracks on and embedded in biopolymer materials. *J. Mater. Chem.* **2011**, *21* (8), 2671−2678.

(17) Yuk, H.; Lu, B.; Lin, S.; Qu, K.; Xu, J.; Luo, J.; Zhao, X. 3D printing of conducting polymers. *Nat. Commun.* **2020**, *11* (1), 1604.

(18) Lu, B.; Yuk, H.; Lin, S.; Jian, N.; Qu, K.; Xu, J.; Zhao, X. Pure PEDOT:PSS hydrogels. *Nat. Commun.* **2019**, *10* (1), 1043.

(19) Wei, H.; Lei, M.; Zhang, P.; Leng, J.; Zheng, Z.; Yu, Y. Orthogonal photochemistry-assisted printing of 3D tough and stretchable conductive hydrogels. *Nat. Commun.* **2021**, *12* (1), 2082.

(20) Ouyang, J. Secondary Doping" methods to significantly enhance the conductivity of PEDOT:PSS for its application as transparent electrode of optoelectronic devices. *Displays* **2013**, *34* (5), 423−436.

(21) Kroon, R.; Mengistie, D. A.; Kiefer, D.; Hynynen, J.; Ryan, J. D.; Yu, L.; Müller, C. Thermoelectric plastics: from design to synthesis, processing and structure-property relationships. *Chem. Soc. Rev.* **2016**, *45* (22), 6147−6164.

(22) Shi, H.; Liu, C.; Jiang, Q.; Xu, J. Effective Approaches to Improve the Electrical Conductivity of PEDOT:PSS: A Review. *Adv. Electron. Mater.* **2015**, *1* (4), 1500017.

(23) Zhang, P.; Aydemir, N.; Alkaisi, M.; Williams, D. E.; Travas-Sejdic, J. Direct Writing and Characterization of Three-Dimensional Conducting Polymer PEDOT Arrays. *ACS Appl. Mater. Interfaces* **2018**, *10* (14), 11888−11895.

(24) Kee, S.; Haque, M. A.; Corzo, D.; Alshareef, H. N.; Baran, D. Self-Healing and Stretchable 3D-Printed Organic Thermoelectrics. *Adv. Funct. Mater.* **2019**, *29* (51), 1905426.

(25) Wang, G.; Huang, W.; Eastham, N. D.; Fabiano, S.; Manley, E. F.; Zeng, L.; Wang, B.; Zhang, X.; Chen, Z.; Li, R.; Chang, R. P. H.; Chen, L. X.; Bedzyk, M. J.; Melkonyan, F. S.; Facchetti, A.; Marks, T. J. Aggregation control in natural brush-printed conjugated polymer films and implications for enhancing charge transport. *Proc. Natl. Acad. Sci. U. S. A.* **2017**, *114* (47), E10066−E10073.

(26) Worfolk, B. J.; Andrews, S. C.; Park, S.; Reinspach, J.; Liu, N.; Toney, M. F.; Mannsfeld, S. C. B.; Bao, Z. Ultrahigh electrical conductivity in solution-sheared polymeric transparent films. *Proc. Natl. Acad. Sci. U. S. A.* **2015**, *112* (46), 14138−14143.

(27) Wang, Y.; Sun, L.; Wang, C.; Yang, F.; Ren, X.; Zhang, X.; Dong, H.; Hu, W. Organic crystalline materials in flexible electronics. *Chem. Soc. Rev.* **2019**, *48* (6), 1492−1530.

(28) Hinckley, A. C.; Andrews, S. C.; Dunham, M. T.; Sood, A.; Barako, M. T.; Schneider, S.; Toney, M. F.; Goodson, K. E.; Bao, Z. Achieving High Thermoelectric Performance and Metallic Transport in Solvent-Sheared PEDOT:PSS. *Adv. Electron. Mater.* **2021**, *7* (3), 2001190.

(29) Mezger, T. G. *The Rheology Handbook*, 2nd ed.; Vincentz Network, 2006.

(30) Kim, S.; Na, S. I.; Jo, J.; Tae, G.; Kim, D. Y. Efficient Polymer Solar Cells Fabricated by Simple Brush Painting. *Adv. Mater.* **2007**, *19* (24), 4410−4415.

(31) Schaffner, M.; Rühs, P. A.; Coulter, F.; Kilcher, S.; Studart, A. R. 3D printing of bacteria into functional complex materials. *Sci. Adv.* **2017**, *3* (12), No. eaao6804.

(32) Palumbiny, C. M.; Liu, F.; Russell, T. P.; Hexemer, A.; Wang, C.; Müller-Buschbaum, P. The Crystallization of PEDOT:PSS Polymeric Electrodes Probed In Situ during Printing. *Adv. Mater.* **2015**, *27* (22), 3391−3397.

(33) Lee, Y. Y.; Choi, G. M.; Lim, S. M.; Cho, J. Y.; Choi, I. S.; Nam, K. T.; Joo, Y. C. Growth Mechanism of Strain-Dependent Morphological Change in PEDOT:PSS Films. *Sci. Rep.* **2016**, *6* (1), 25332.

https://doi.org/10.1021/acsapm.3c00232
ACS Appl. Polym. Mater. XXXX, XXX, XXX−XXX

(34) Greczynski, G.; Kugler, T.; Salaneck, W. R. Characterization of the PEDOT-PSS system by means of X-ray and ultraviolet photoelectron spectroscopy. *Thin Solid Films* **1999**, *354* (1), 129−135.
(35) Yemata, T. A.; Zheng, Y.; Kyaw, A. K. K.; Wang, X.; Song, J.; Chin, W. S.; Xu, J. Modulation of the doping level of PEDOT:PSS film by treatment with hydrazine to improve the Seebeck coefficient. *RSC Adv.* **2020**, *10* (3), 1786−1792.
(36) Park, H.; Lee, S. H.; Kim, F. S.; Choi, H. H.; Cheong, I. W.; Kim, J. H. Enhanced thermoelectric properties of PEDOT:PSS nanofilms by a chemical dedoping process. *J. Mater. Chem. A* **2014**, *2* (18), 6532−6539.
(37) Diah, A. W. M.; Quirino, J. P.; Belcher, W.; Holdsworth, C. I. Investigation of the doping efficiency of poly(styrene sulfonic acid) in poly(3,4-ethylenedioxythiophene)/poly(styrene sulfonic acid) dispersions by capillary electrophoresis. *Electrophoresis* **2014**, *35* (14), 1976−1983.
(38) Ouyang, L.; Musumeci, C.; Jafari, M. J.; Ederth, T.; Inganäs, O. Imaging the Phase Separation Between PEDOT and Polyelectrolytes During Processing of Highly Conductive PEDOT:PSS Films. *ACS Appl. Mater. Interfaces* **2015**, *7* (35), 19764−19773.
(39) Zhang, Y. S.; Yue, K.; Aleman, J.; Mollazadeh-Moghaddam, K.; Bakht, S. M.; Yang, J.; Jia, W.; Dell'Erba, V.; Assawes, P.; Shin, S. R.; Dokmeci, M. R.; Oklu, R.; Khademhosseini, A. 3D Bioprinting for Tissue and Organ Fabrication. *Ann. Biomed Eng.* **2017**, *45* (1), 148−163.
(40) Martelli, N.; Serrano, C.; van den Brink, H.; Pineau, J.; Prognon, P.; Borget, I.; El Batti, S. Advantages and disadvantages of 3-dimensional printing in surgery: A systematic review. *Surgery* **2016**, *159* (6), 1485−1500.
(41) Mannoor, M. S.; Jiang, Z.; James, T.; Kong, Y. L.; Malatesta, K. A.; Soboyejo, W. O.; Verma, N.; Gracias, D. H.; McAlpine, M. C. 3D Printed Bionic Ears. *Nano Lett.* **2013**, *13* (6), 2634−2639.
(42) Mawad, D.; Stewart, E.; Officer, D. L.; Romeo, T.; Wagner, P.; Wagner, K.; Wallace, G. G. A Single Component Conducting Polymer Hydrogel as a Scaffold for Tissue Engineering. *Adv. Funct. Mater.* **2012**, *22* (13), 2692−2699.
(43) Kaur, G.; Adhikari, R.; Cass, P.; Bown, M.; Gunatillake, P. Electrically conductive polymers and composites for biomedical applications. *RSC Adv.* **2015**, *5* (47), 37553−37567.
(44) Ling, Y.; An, T.; Yap, L. W.; Zhu, B.; Gong, S.; Cheng, W. Disruptive, Soft, Wearable Sensors. *Adv. Mater.* **2020**, *32* (18), 1904664.
(45) Ma, Y.; Zhang, Y.; Cai, S.; Han, Z.; Liu, X.; Wang, F.; Cao, Y.; Wang, Z.; Li, H.; Chen, Y.; Feng, X. Flexible Hybrid Electronics for Digital Healthcare. *Adv. Mater.* **2020**, *32* (15), 1902062.
(46) Kleinschmidt, A. T.; Lipomi, D. J. Stretchable Conjugated Polymers: A Case Study in Topic Selection for New Research Groups. *Acc. Chem. Res.* **2018**, *51* (12), 3134−3143.
(47) Kayser, L. V.; Lipomi, D. J. Stretchable Conductive Polymers and Composites Based on PEDOT and PEDOT:PSS. *Adv. Mater.* **2019**, *31* (10), 1806133.
(48) Greer, J. R.; Deshpande, V. S. Three-dimensional architected materials and structures: Design, fabrication, and mechanical behavior. *MRS Bull.* **2019**, *44* (10), 750−757.
(49) Hinton, T. J.; Jallerat, Q.; Palchesko, R. N.; Park, J. H.; Grodzicki, M. S.; Shue, H. J.; Ramadan, M. H.; Hudson, A. R.; Feinberg, A. W. Three-dimensional printing of complex biological structures by freeform reversible embedding of suspended hydrogels. *Sci. Adv.* **2015**, *1* (9), No. e1500758.
(50) Gong, J.; Schuurmans, C. C. L.; van Genderen, A. M.; Cao, X.; Li, W.; Cheng, F.; He, J. J.; López, A.; Huerta, V.; Manríquez, J.; Li, R.; Li, H.; Delavaux, C.; Sebastian, S.; Capendale, P. E.; Wang, H.; Xie, J.; Yu, M.; Masereeuw, R.; Vermonden, T.; Zhang, Y. S. Complexation-induced resolution enhancement of 3D-printed hydrogel constructs. *Nat. Commun.* **2020**, *11* (1), 1267.
(51) Oran, D.; Rodriques, S. G.; Gao, R.; Asano, S.; Skylar-Scott, M. A.; Chen, F.; Tillberg, P. W.; Marblestone, A. H.; Boyden, E. S. 3D nanofabrication by volumetric deposition and controlled shrinkage of patterned scaffolds. *Science* **2018**, *362* (6420), 1281−1285.
(52) Dickey, M. D. Stretchable and Soft Electronics using Liquid Metals. *Adv. Mater.* **2017**, *29* (27), 1606425.

https://doi.org/10.1021/acsapm.3c00232
ACS Appl. Polym. Mater. XXXX, XXX, XXX−XXX